U.S. DEPARTMENT OF ENERGY

PNNL-23313

Prepared for the U.S. Department of Energy
under Contract DE-AC05-76RL01830

Rolling Process Modeling Report: Finite-Element Prediction of Roll-Separating Force and Rolling Defects

A Soulami
CA Lavender
DM Paxton
DE Burkes

April 2014

Pacific Northwest
NATIONAL LABORATORY

Proudly Operated by Battelle *Since 1965*

PACIFIC NORTHWEST NATIONAL LABORATORY
operated by
BATTELLE
for the
UNITED STATES DEPARTMENT OF ENERGY
under Contract DE-AC05-76RL01830

Printed in the United States of America

Available to DOE and DOE contractors from the
Office of Scientific and Technical Information,
P.O. Box 62, Oak Ridge, TN 37831-0062;
ph: (865) 576-8401
fax: (865) 576-5728
email: reports@adonis.osti.gov

Available to the public from the National Technical Information Service
5301 Shawnee Rd., Alexandria, VA 22312
ph: (800) 553-NTIS (6847)
email: orders@ntis.gov <http://www.ntis.gov/about/form.aspx>
Online ordering: http://www.ntis.gov

This document was printed on recycled paper.
(8/2010)

PNNL-23313

Rolling Process Modeling Report: Finite-Element Prediction of Roll-Separating Force and Rolling Defects

A Soulami
CA Lavender
DM Paxton
DE Burkes

April 2014

Prepared for
the U.S. Department of Energy
under Contract DE-AC05-76RL01830

Pacific Northwest National Laboratory
Richland, Washington 99352

Abstract

Pacific Northwest National Laboratory (PNNL) has been investigating manufacturing processes for the uranium-10% molybdenum (U-10Mo) alloy plate-type fuel for high-performance research reactors in the United States. This work supports the Convert Program of the U.S. Department of Energy's National Nuclear Security Administration (DOE/NNSA) Global Threat Reduction Initiative. This report documents modeling results of PNNL's efforts to perform finite-element simulations to predict roll-separating forces and rolling defects. Simulations were performed using a finite-element model developed using the commercial code LS-Dyna. Simulations of the hot rolling of U-10Mo coupons encapsulated in low-carbon steel have been conducted following two different schedules. Model predictions of the roll-separation force and roll-pack thicknesses at different stages of the rolling process were compared with experimental measurements. This report discusses various attributes of the rolled coupons revealed by the model (e.g., dog-boning and thickness non-uniformity). Model predictions were validated and further development will allow accurate specification of rolling schedules for production roll mills based on the testing of laboratory scale mills.

Acknowledgments

Roll-separation force data was obtained from experiments conducted at the Idaho National Laboratory during 2008. The authors would like to acknowledge those that were involved with the experiments and collection of the raw data, including Mr. Glenn Moore, Mr. Blair Park, Mrs. Francine Rice, and Mr. Steve Steffler. The authors appreciate the opportunity to use the roll-separation force data to validate the model presented here.

Acronyms and Abbreviations

FEM	finite-element model
HEU	high-enriched uranium
LEU	low-enriched uranium
PNNL	Pacific Northwest National Laboratory
UTS	ultimate tensile stress

Contents

Figures

Tables

1.0 Introduction

Transition from high-enriched uranium (HEU) fuel to low-enriched uranium (LEU) fuel in research and test reactors has been a global focus for the past three decades (Snelgrove, et al. 1997). The Global Threat Reduction Initiative Reactor Convert Program is currently considering uranium alloyed with nominally 10 wt% molybdenum (U-10Mo) as a monolithic LEU fuel with the potential to enable the conversion of high-performance research and test reactors from the use of HEU fuels. In U-10Mo, the molybdenum in the uranium alloy stabilizes the cubic gamma phase allowing for acceptable irradiation and swelling behavior under irradiation (Lee et al. 1997, Park et al. 2001, Meyer et al. 2002, Ozaltun et al. 2011). A monolithic U-10Mo foil encapsulated in aluminum alloy cladding possesses the greatest possible LEU density in the fuel region, maintains excellent resistance to anisotropic growth (i.e., swelling), and is compatible with existing reactor designs. In addition, the U-10Mo fuel alloy represents a good combination of irradiation performance, oxidation resistance, strength, and ductility. Therefore, it is ideal for reducing nuclear proliferation risks associated with the transportation and storage of large quantities of HEU.

Extensive research has been conducted regarding process-variable relationships during hot rolling and methods to predict changes in resultant sheet metal characteristics. However, a majority of this research has focused on conventional structural metals (e.g., steel) and little research exists on development of predictive tools that can be applied to hot rolling of uranium alloys and even less for rolling of encapsulated coupons. When designing hot-rolling schedules, particularly for roll-packs, the ability to quickly investigate the influence of process variables on properties (e.g., roll-separation force) and possible defects (e.g., thickness uniformity, dog-boning, waviness, etc.) is highly desirable. Understanding these properties is important for optimizing the process efficiency, achieving desired foil quality, engineering the desired foil characteristics, and developing reasonable production schedules on a rational scientific basis.

Several studies have been conducted on the defects created during hot rolling. Komori (1988) investigated shape defects called “cross buckling” or “vertical buckling” that sometimes appear during hot rolling. He demonstrated that the cause of the vertical and cross buckling is the residual stress distribution near the exit cross section outside the roll gap. In a second study, He investigated the mechanisms of the herring-bone and reduction-mark defects in sheet rolling using experiments and analytical models (Komori 1996).

Non-uniformity of thickness is one of the most common issues associated with rolling. Thickness can vary along the length of the rolled strip as well as across its width. Longitudinal changes in thickness are caused by variations in incoming thickness, friction, hardness, temperature, etc., along the rolled strip. Variations in these factors are even more pronounced in the case of coupons encapsulated in cans composed of a picture frame with top and bottom covers. This configuration causes variations in roll-separation force and, thus, in the thickness,

which is proportional to the pressure applied on the rolled sheet pack. Variations in thickness across the width are generally caused by roll flattening and roll bending under load (Avitzur, 1982). This variation can also be caused by the geometry of the roll-pack, with a significant mismatch of strength between the middle area where the coupon is located and near the edges of the picture frame where only can material is present.

The second rolling defect considered in this study is "dog-boning." This end effect refers to a localized thickening of the fuel alloy and thinning of the cladding at the edges of the fuel core. In the case of aluminum-clad material, it was demonstrated that dog-boning is a result of the marked difference in plasticity between the high-uranium core alloy and the aluminum containment materials at the elevated temperature required for rolling (Thurber and Beaver 1959). This defect was also observed in our previous work where U-10Mo coupons inside 1018 steel cans were hot rolled into thin foils (Soulami et al. 2013). Pasqualini (2008) presented a study showing very little dog-boning while hot rolling U-10Mo coupons inside Zr cans. This is in accordance with the theory that less difference in strength between the core material and the cladding material leads to more uniform deformation.

Waviness of the rolled sheet pack also is a parameter of utmost interest to any rolling engineer, because it often becomes critical for the acceptance or rejection of the rolled flat products. This defect can result from various aspects of the rolling process such as bending of the rolls and changes in the roll-separation force along the sheet pack. Waviness also can be a consequence of dog-boning and possible gaps between the core coupon and the picture frame.

This report presents a study investigating the mechanical behavior of a roll-pack during the hot-rolling process. The roll-pack used in this study consisted of a U-10Mo ingot (termed "coupon") encapsulated in a low-carbon steel (AISI 1018) can. A finite-element model (FEM) of the rolls and roll-pack was developed using the commercial code LS-DYNA.

The first step in any FEM process is to ascertain accurate mechanical properties of the materials. Thermo-physical properties and alloy-preparation methods of U-10Mo have been studied in detail by Burkes et al. (2009, 2010). In addition, compression tests were performed on U10Mo samples at PNNL and results were reported by Joshi et al. (2013). In the absence of actual measurements of the roll-pack temperature during experiments, temperature calculations were carried out based on previously developed analytical methods (Seredynski 1973). Note that temperatures predicted by the analytical methods appeared reasonable with the assumptions that were made. Those temperatures were used in the current study to apply the appropriate temperature boundary conditions of the roll-pack at every pass and select the mechanical properties as an input to the FEM. As a validation step, predicted roll-separation forces were compared to experimental measurements. Two rolling schedules, with different reduction rates and heating sequences, were considered in this study. Simulations permit investigation of various aspects of the roll-pack shape such as dog-boning and thickness variation.

This study also investigates distortion in the U-10Mo sheet pack during hot rolling using FEM simulations. Four cases were considered: 1) rolling of U-10Mo coupon inside a 1018 steel can, 2) rolling of U-10Mo coupon inside a 304 stainless steel can, 3) rolling of U-10Mo coupon inside a Zircaloy-2 can, and 4) bare rolling of a U-10Mo coupon. Simulation results are presented and discussed with a focus on the rolling defects discussed earlier (thickness uniformity, dog-boning, and waviness).

It is anticipated that this model, along with the temperature calculation proposed herein, will be used in subsequent studies to help determine optimal parameters (e.g., temperature control, hot-rolling temperature, number of passes, reduction rates, roll diameters, etc.) for thermo-mechanical processing and fabrication of U-Mo fuel foils encapsulated in a roll-pack.

2.0 Process Description and Sample Geometry

The fabrication process for hot rolling of U-10Mo coupons uses a picture-frame-type roll-pack fabricated from low-carbon steel or Zr plate material. Fuel foils simulated for this work were prepared similarly to those used in Moore and Marshall (2010)). Roll-packs consisted of an inner-picture-frame piece around the periphery of the U-10Mo and a top and bottom cover plate. The thickness of the inner portion of the frame was sized to the same thickness as the U-10Mo alloy coupon. Figure 1 represents a schematic view of the full roll-pack. The alloy coupon dimensions are nominally 29.5 mm long × 18.6 mm wide × 2.72 mm thick. The outer dimensions of the roll-pack frame are nominally 19.1 mm greater in both length and width than that of the coupon. The thicknesses of the cover plates are nominally 3.34 mm. Note that there is a clearance of ~0.23 mm between the alloy coupon and the picture frame. Coupons of this size produce mini-foils, whereas larger coupons to be used in production will result in increased roll-separation forces depending upon the configuration of the rolling mill. The roll-pack was preheated and reheated in a box furnace set at a constant temperature of 650°C. After being removed from the furnace, the roll-pack was given one to five passes, as quickly as possible, through the rolling mill as dictated by the specific rolling schedule. After reheating, this process is repeated several times. The rolls used in this setup were 25.4 cm in diameter and 25.4 cm wide with a rotation velocity of 10 revolutions per minute (rpm) which corresponds to 1.047 radians per second (rad/s). This equates to a translational velocity of 133 mm/s at the entrance of the rolls.

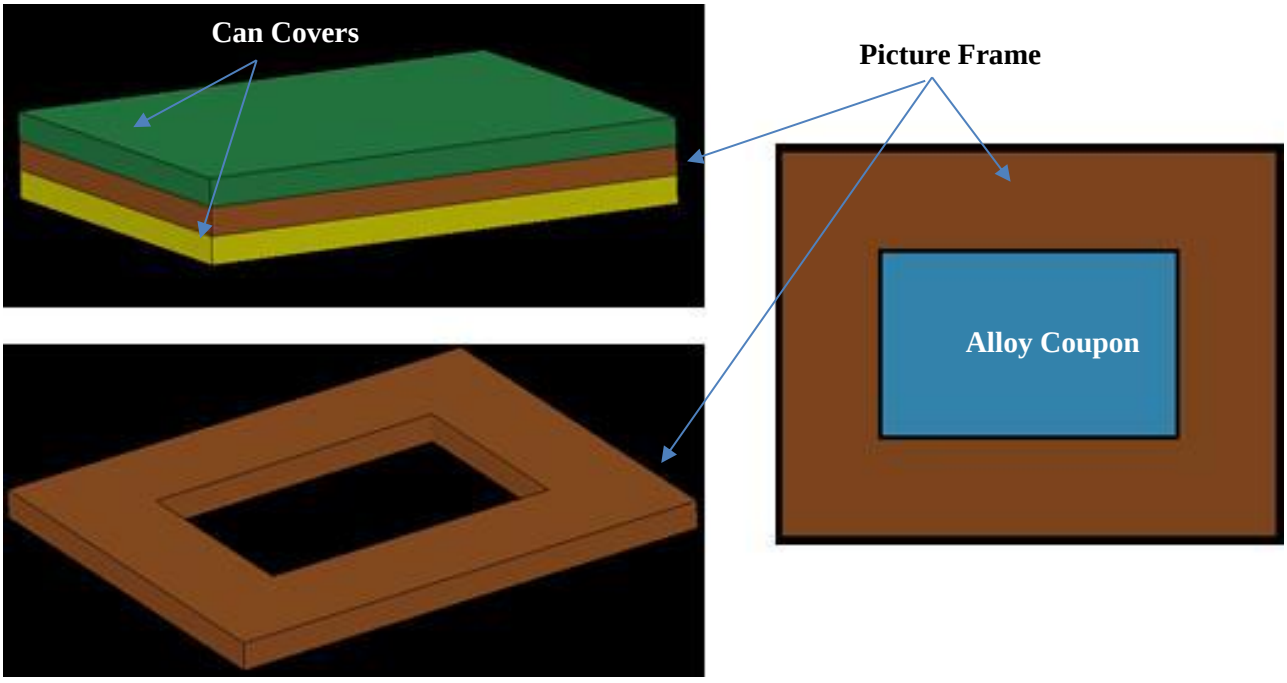

Figure 1. Representation of the Full Roll-Pack. The blue area represents the alloy coupon, the green area is the top cover of the can, the yellow area is the bottom cover of the can, and the brown area is the frame.

3.0 FEM Model Description and Material Properties

3.1 Model Description and Geometry

The present study used FEM-based commercial software, LS-DYNA, to simulate the hot rolling of LEU fuel foils. Coupled thermal-structural analysis, using elastic-plastic-thermal constitutive equations, was adopted to describe the material behavior. To reduce the size of the model and due to the symmetry of the geometry of the roll-pack and the rolls, only half of the setup was modeled. The symmetry plane was chosen to be the mid-plane, cutting the roll-pack in half lengthwise and, to account for the symmetry, appropriate boundary conditions were applied. The rolling setup consisted of two rolls and a roll-pack made up of a coupon and the can material. Rolls were 25.4 cm in diameter and 25.4 cm wide and considered rigid and non-distorting. Table 1 summarizes the dimensions for the alloy coupon and roll-pack.

Table 1. Physical Dimensions (mm) of Alloy Coupon and Roll-Pack used in the Current Study

Alloy Coupon	Thickness	2.72
	Width	18.6
	Length	29.5
Roll-pack	Thickness	9.40
	Width	37.7
	Length	48.5

The rolls were modeled using 51,072 rigid shell elements (for the half model); with an initial mesh size of ~2 × 2 mm. The roll-pack was modeled using three-dimensional (3D) 69,649 brick elements with an initial mesh size of ~0.5 × 0.5 × 0.5 mm. The actual roll assembly is welded along the perimeter to form the can. In the model, the welded region was considered to have the same mechanical properties as the parent can material. However, to account for the weld, the outer layer of elements in contact with the top cover, picture frame, and bottom cover of the can are tied to each other in order to account for the weld. For this purpose, the coincident nodes of these elements have been merged. Figure 2 shows different views of the half model. The roll-pack is shown at the entrance in between the rolls.

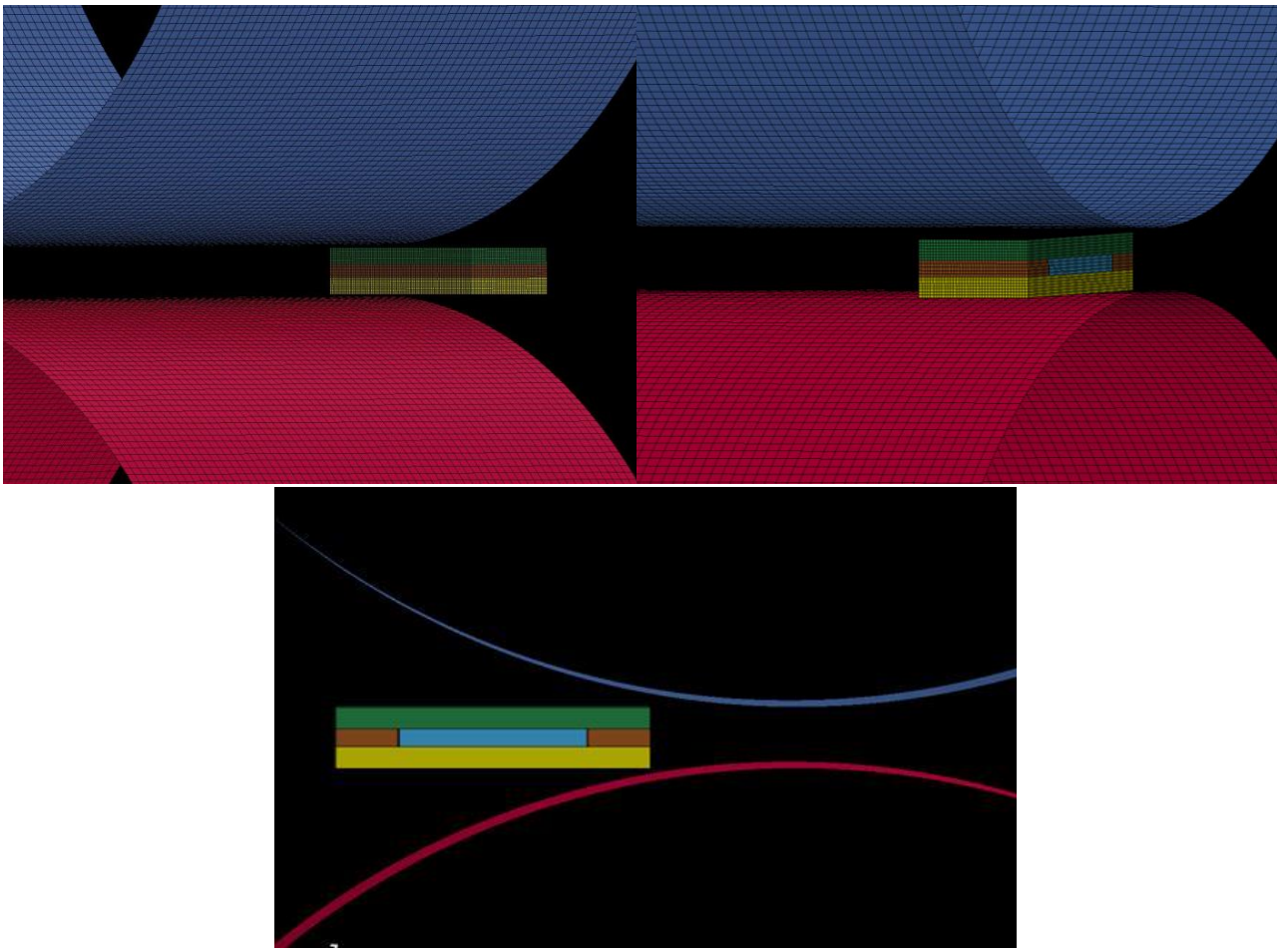

Figure 2. Different Views of the FEM Model (half)

Several contact algorithms available in LS-DYNA were tested and *AUTOMATIC_SURFACE_TO_SURFACE_THERMAL with a friction coefficient of 0.35 was selected. This contact algorithm was also used to predict the heat transfer due to conduction between the roll-pack and the rolls. While the rolls are considered as rigid material in this study, the can (low-carbon steel, AISI 1018) and the alloy coupon (U-10Mo) were modeled using *MAT_ELASTIC_PLASTIC_THERMAL in LS-DYNA. This constitutive model is temperature-dependent and suited to model isotropic plasticity at high temperatures. This elastic-plastic model is computationally efficient and only needs a few parameters. The difference between yield stress and the ultimate tensile stress (UTS) with strain were used to determine the plastic hardening moduli of the material.

A rotation velocity of 10 revolutions per minute (rpm) was assigned to the rolls, which corresponds to 1.047 radians per second (rad/s). This equates to a translational velocity of 133 mm/s at the entrance of the rolls. This velocity was applied to the roll-pack using the card *INITIAL_VELOCITY in LS-DYNA. Once a roll-pack exits the rolls after a pass, the

simulation stops and a restart file is created. This restart file is used to map the deformations, stresses, and temperatures on the roll-pack before simulating the next pass. Note that, based on the actual temperature of the roll-pack the model will automatically update the material properties for the U-10Mo and steel can. Rolls rotation sense and linear velocity direction are flipped so the roll-pack enters the rolls for the next pass with the desired reduction rate from the opposite side of the rolls. These steps are repeated for each pass until completion of the desired schedule.

3.2 Temperature Boundary

Temperature is one of the most important parameters of the hot-rolling process. Temperature is critical for determining the material properties of the alloy coupon and the can, particularly because multiple passes are made between reheating. Temperature loss from the roll-pack is considered to result from heat conduction from the roll-pack to the work rolls and from radiation of the roll-pack to the ambient surrounding. Temperature loss can also occur via convection. However, given the rapid transfer times (<10 s) and the difficulty in calculation, temperature loss due to convection was not considered here.

Several past studies demonstrated that the coupled thermal-structure analysis in LS-DYNA can adequately reproduce different hot-forming processes. Shapiro (2007, 2009) presented studies on hot-forming and hot-stamping simulations using LS-DYNA. D'amours and Bréland (2011) developed a finite-element model that predicts the necessary tube temperature and gas pressure during the heat-based forming process. The present model implements temperature loss through radiation boundary conditions and within the contact definition to account for the heat conduction between the roll-pack and the rolls. Rolls are heated to an initial temperature of 50°C whereas the surrounding ambient temperature is 25°C. To simulate the temperature loss during the transfer of the roll-pack from the furnace/exit rolls into the rolls entrance, steps to simulate radiation are necessary. During these steps, between every two passes, only heat loss due to radiation with ambient surrounding is considered. To optimize computation time, and using data from the experiments, an average temperature loss is calculated and applied to the roll-pack as an initial temperature boundary condition after every pass. This temperature loss is time-dependent (i.e., the time required for the catcher to pass the roll-pack back to the pitcher). The temperature loss, ΔT_R, is determined using Equation 1 with units of $^{o}C \bullet sec^{-1}$ following the process described by Seredynski (2007).

$$\Delta T_r = -\frac{2\psi\xi}{\rho c h_m} T^4 \Delta t \qquad (1)$$

where ψ is the Stefan-Boltzmann constant, ξ is the emissivity of the roll-pack (oxidized), T is the temperature of the roll-pack prior to exiting the furnace or upon exiting the rolls, ρc is the

temperature-dependent volumetric heat capacity of the roll-pack, Δt is the elapsed time between removal from the furnace or work rolls and insertion of the roll-pack into the work rolls, and h_m is the thickness of the roll-pack prior to the reduction pass. Equation 1 is based on three basic assumptions: 1) the ambient temperature is neglected (i.e., $T >> T_a$), 2) the geometry of the roll-pack represents a plate (i.e., $b_m >> h_m$ and $l >> h_m$), and 3) short time intervals are considered (i.e., $\Delta t < 20$ sec). All three assumptions are valid for this study. In addition, heat gain due to plastic deformation is modeled during deformation, even though the temperature rise is not very significant compared to the rolling temperature.

Figure 3 shows a flowchart of temperature transfers throughout the rolling process.

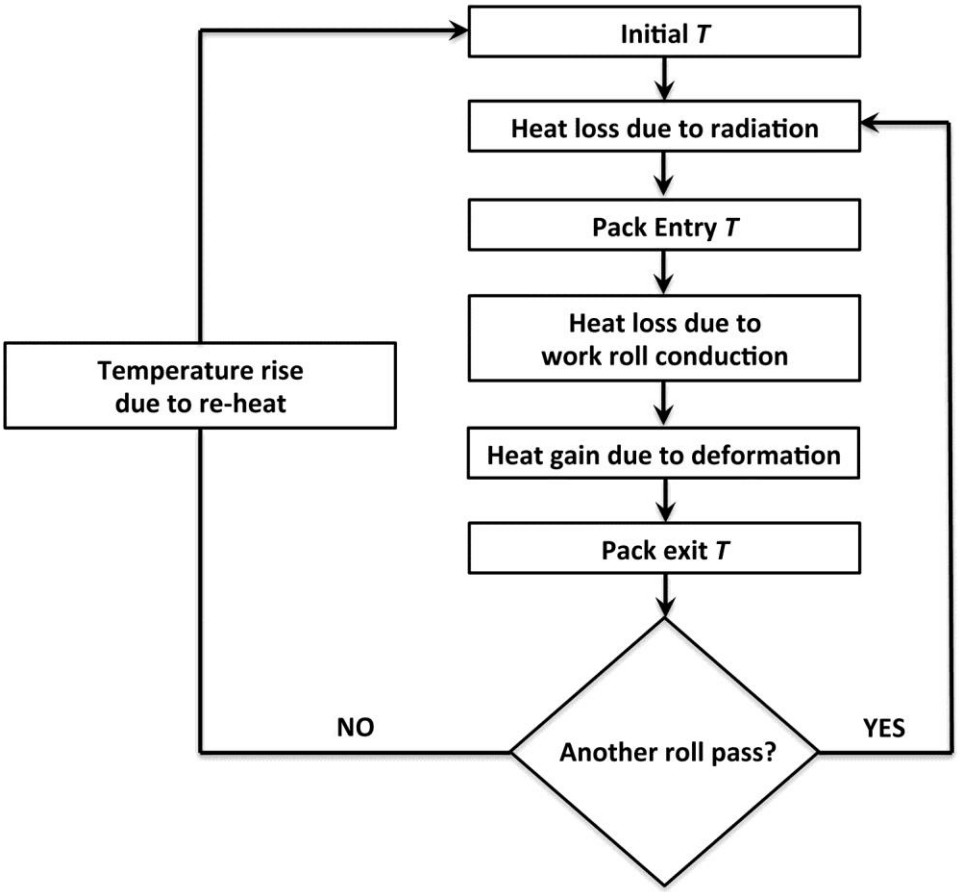

Figure 3. Flowchart of the Rolling Process

3.3 Material Properties

Four rolling scenarios are considered in the present work: 1) rolling of a U-10Mo coupon in a 1018 low-carbon steel can, 2) rolling of a U-10Mo coupon in a 304 Stainless Steel can, 3) rolling of a U-10Mo coupon in a Zr can, and 4) rolling of a U-10Mo coupon with no can material termed "bare rolling." Model input included temperature-dependent tensile properties of U-10Mo, low-carbon steel AISI 1018, 304 stainless steel, and Zircaloy-2. Figure 4 provides tensile strength as a function of temperature for U-10Mo from various sources, including McPherson (1958), Farkas (1967), Waldron et al. (1958), and AN-176 (1960). A linear best-fit correlation through selected data (Equation 2) is assumed to represent the temperature-dependent tensile strength of a U-10Mo alloy from room temperature up to 750°C.

$$\sigma_{y,U-10Mo}(T) = 933.7 - 1.041T \tag{2}$$

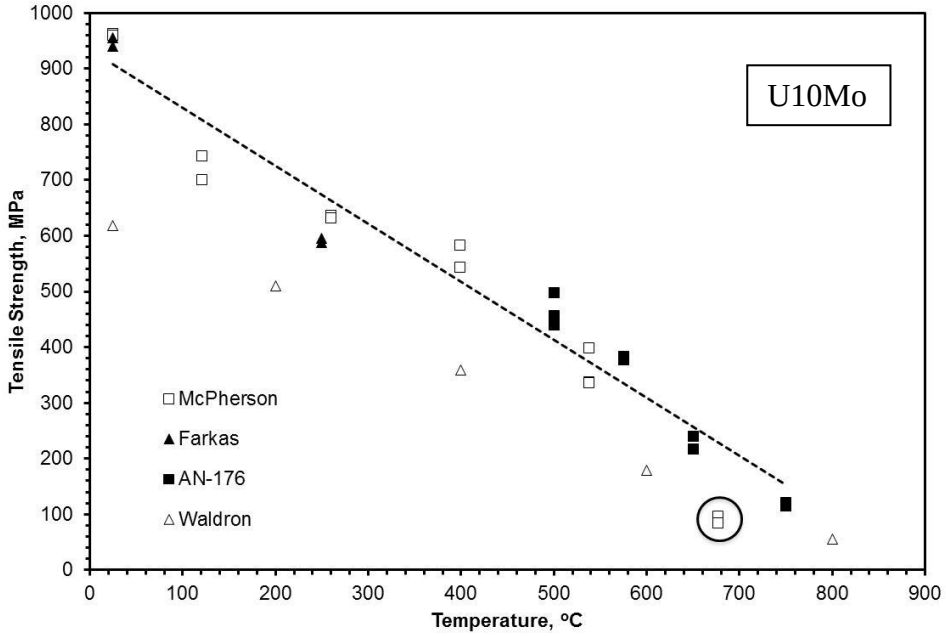

Figure 4. Temperature-Dependent Tensile Strength Data of U-10Mo alloy. Solid and open shapes represent Yield Stress and UTS, respectively.

AISI 1018 and 304 stainless steel tensile properties at different temperatures are presented in Figure 5 and Figure 6 respectively, whereas Zircaloy-2 tensile properties as a function of temperature are presented in Figure 7. Note that the tensile strength of Zircaloy-2 can be significantly increased (with reduction in ductility) when the material is cold worked. In Whitmarsh's report (Whitmarsh 1962), as a comparison with annealed material mechanical properties, we can see that the UTS is 50% higher when Zircaloy-2 is submitted to 10% cold

work. The yield strength is 70% higher in this case. At elevated temperature, this ratio is even higher. At 600 °C, UTS is 70% higher and yield strength is 140% higher. This increase in strength was also demonstrated to be higher when the material is submitted to 15-50% cold work.

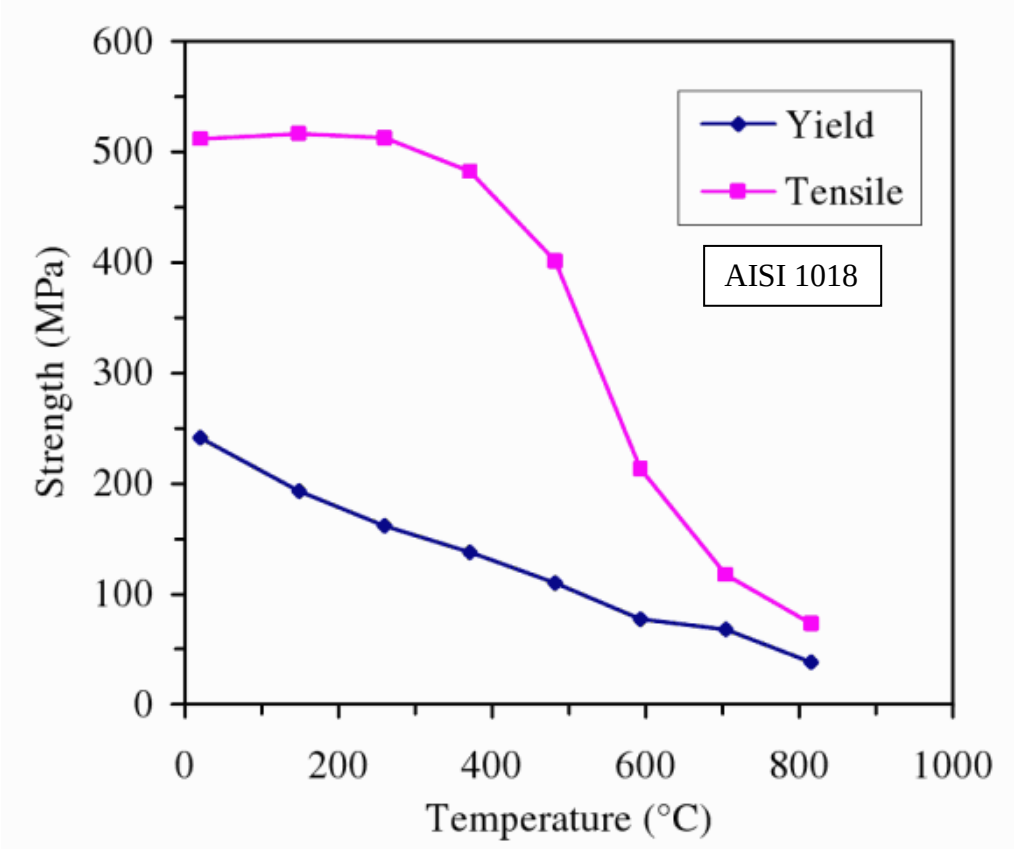

Figure 5. Temperature-Dependent Tensile Strength Data of AISI 1018 (Clauss 1969)

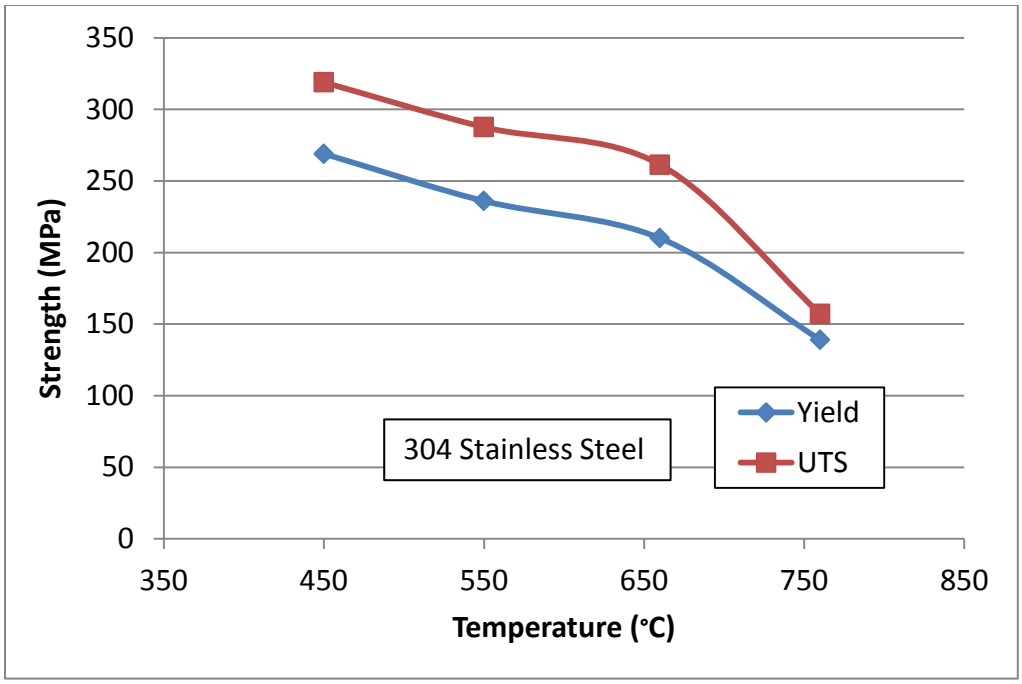

Figure 6. Temperature-Dependent Tensile Strength Data of 304 Stainless Steel (Chen and Young 2006)

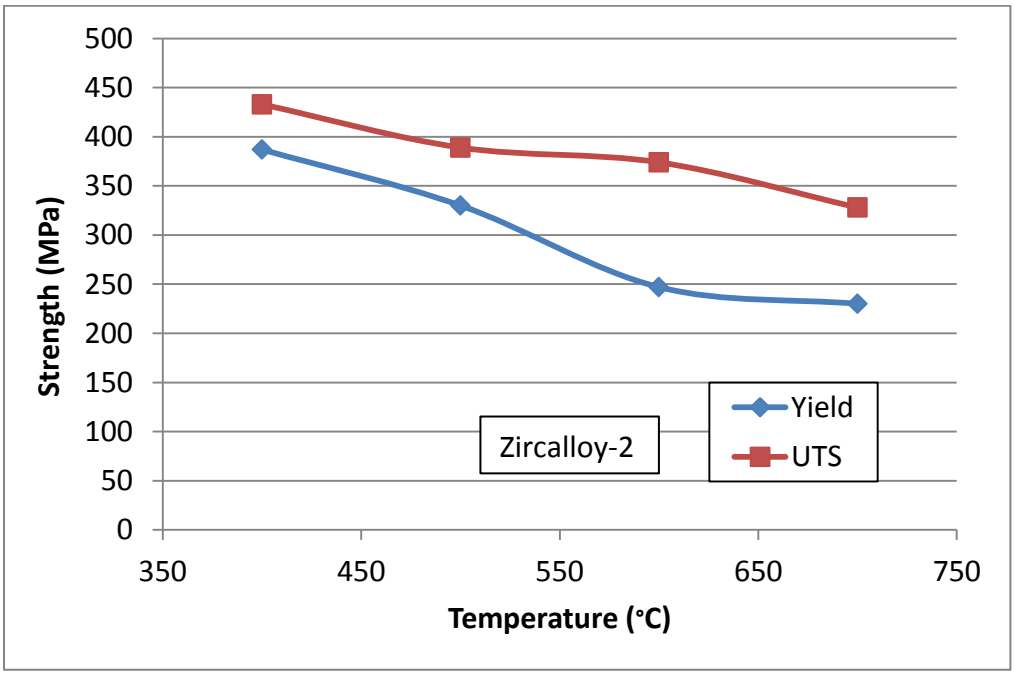

Figure 7. Temperature-Dependent Tensile Strength Data of 304 Stainless Steel (Chen and Young 2006)

All other thermo-mechanical parameters used as an input to the model are summarized in Table 2. Note that these parameters are considered constant with respect to temperature in the 400 to 650°C range. Peterson and Vandervoort (1964) stated that U-10Mo does not undergo work-hardening during deformation in this temperature range. However, compression tests, done at PNNL and reported in Joshi et al. (2013), show that at a particular strain rate, compression samples that were tested below the eutectoid temperature (550°C) showed significantly higher yield stress and flow stress as compared to those that were compression tested above the eutectoid temperature by over 50%. In other words, significant work-hardening is present at temperatures below (550°C). Figure 8 represents the true stress-strain curves at different temperatures for U-10Mo tested under compression.

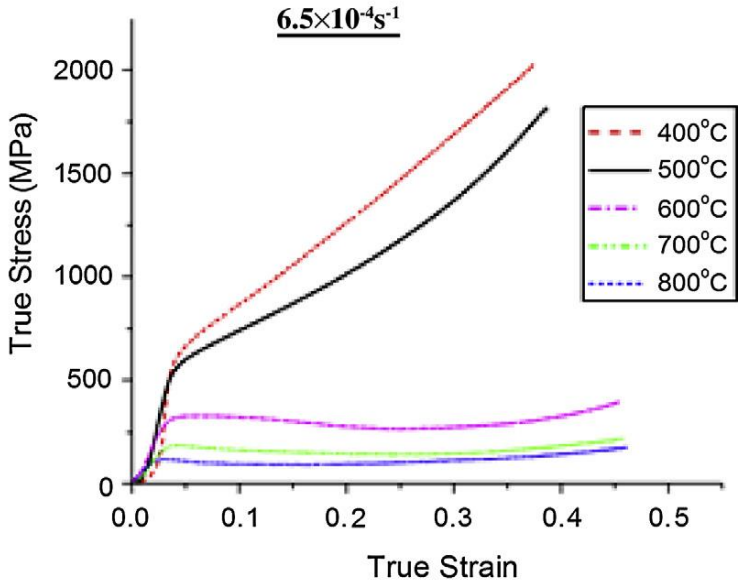

Figure 8. Stress-Strain Curves for U-10Mo Compression Tested at Different Temperatures

For U-10Mo, AISI 1018, 304 stainless steel, and Zircaloy-2 an elastic-plastic constitutive model was adopted, with a tangent modulus to account for the work-hardening during deformation.

Table 2. Thermo-Mechanical Properties of U-10Mo, AISI 1018, and Zircaloy-2 (Burkes et al. 2010, Ozaltun et al. 2011, Boyer 1985, Whitmarsh 1962, Chavez et al. 1994)

AISI 1018	
Young Modulus	200,000 MPa
Poisson's Ratio	0.3
Density	7,800 Kg/m^3
Thermal Conductivity	51.9 W/m.C
Heat Capacity	486 J/Kg.C
Coefficient of Thermal Expansion	14.0 10^{-6}m/m.C
304 Stainless Steel	
Young Modulus	200,000 MPa
Poisson's Ratio	0.33
Density	7,800 Kg/m^3
Thermal Conductivity	15.5 W/m.C
Heat Capacity	500 J/Kg.C
Coefficient of Thermal Expansion	17.5 10^{-6}m/m.C
Zircaloy-2	
Young Modulus	96,526 MPa
Poisson's Ratio	0.4
Density	6,530 Kg/m^3
Thermal Conductivity	21.5 W/m.C
Heat Capacity	285 J/Kg.C
Coefficient of Thermal Expansion	6.5 10^{-6}m/m.C
U-10Mo	
Young Modulus	65,000 MPa
Poisson's Ratio	0.35
Density	16,060 Kg/m^3
Thermal Conductivity	35.5 W/m.C
Heat Capacity	167 J/Kg.C
Coefficient of Thermal Expansion	16.4 10^{-6}m/m.C

4.0 Results and Discussions

4.1 Model Validation

4.1.1 Rolling Schedules

Data from experiments involving two different rolling schedules for small alloy coupons were used to validate the model predictions. Each rolling schedule used 15 passes; however, the reduction per pass and reheating schedules varied (see Table 3). The first rolling schedule (Schedule A) involved fewer reheating cycles, more subsequent roll passes between reheats, larger reduction rates per pass early in the schedule, and less time to complete. The second rolling schedule (Schedule B) involved many more reheats, fewer subsequent roll passes between reheats, relatively larger reduction rates per pass late in the schedule, and more time to complete. Table 3 summarizes the reduction rates and roller settings used in Schedules A and B for the first 15 passes.

Table 3. Reduction Rates, Roller Settings, and Reheats for Schedules A and B

Schedule A				Schedule B			
Pass	Reduction Rate	Roller Setting (mm)	Reheats (°C)	Pass	Reduction Rate	Roller Setting (mm)	Reheats (°C)
0		9.39	650	0		9.40	635
1	10%	8.38		1	4.32%	8.99	-
2	10%	7.62		2	4.52%	8.59	640
3	10%	6.85		3	4.73%	8.18	-
4	7%	6.37		4	4.97%	7.77	639
5	7%	5.91	629	5	5.23%	7.37	-
6	7%	5.51		6	5.52%	6.96	639
7	6%	5.18		7	5.84%	6.55	-
8	6%	4.87		8	6.20%	6.15	639
9	6%	4.57		9	6.61%	5.74	-
10	5%	4.34	617	10	7.08%	5.33	639
11	5%	4.14		11	7.62%	4.93	-
12	5%	3.93		12	8.25%	4.52	639
13	5%	3.73		13	8.99%	4.11	-
14	5%	3.53		14	9.88%	3.71	640
15	5%	3.35	591	15	4.32%	3.30	-

4.1.2 Roll-Separating Force

Roll-separating force data was experimentally obtained, through direct measurements, as a function of time for the two different rolling schedules. The experimental measurements presented in Figure 9 were averages of multiple points recorded every 0.2 seconds from insertion of the pack into the mill until the pack exits the mill. Therefore, as the roll-pack increased in length later in the rolling schedule, more data points were recorded. Figure 9 provides an example of a typical roll-separation force profile as a function of time and shows a sharp increase in the roll-separation force to approximately 175 kN, followed by a decrease to approximately 165 kN, followed by an increase to 190 kN that is maintained over roughly 1.5 seconds. A similar sequence was observed as the roll-pack exited the rolling mill. The initial steady-state force of approximately 165 kN was due to rolling of the 1018 steel frame, the next steady-state roll-separation force of 190 kN was due to the contribution of the stronger U-10Mo coupon, and the next region of 165 kN was again due to only the rolling of the 1018 steel frame.

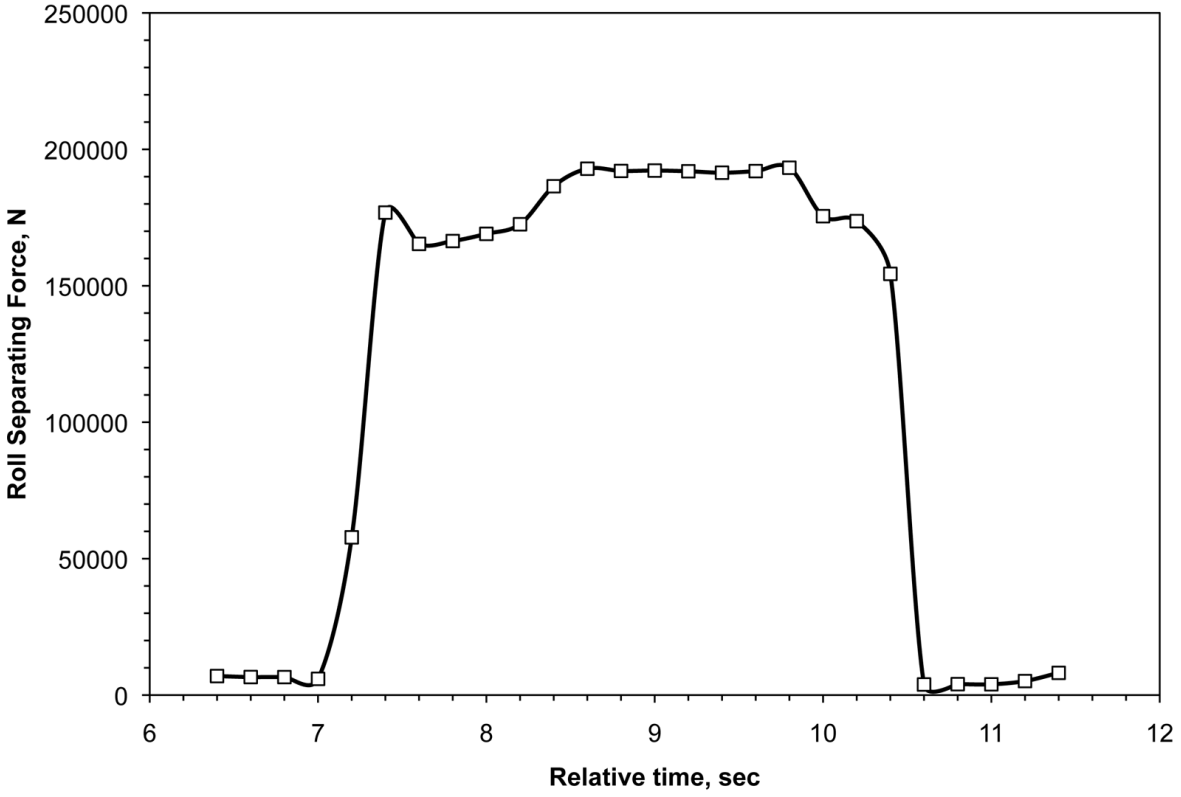

Figure 9. Example of a Typical Roll-Separation Force Profile as a Function of Relative Time

Roll-separating force was also calculated from the model, the average stress in the z-direction at every element of the roll-pack in contact with the rolls was recorded when the roll-pack is halfway through the rolling pass. The roll-separation force is calculated by summing the z-force

for each element that was found multiplying the vertical stress (z-stress) by the respective contact area.

Figure 10 presents a top-down view of the z-stress contours of the roll-pack halfway between the rolls. The contact zone is indicated by a red rectangle. The higher stress area in the contact zone (near the top of Figure 10) is associated with the higher strength U-10Mo, whereas the lower stress (bottom of Figure 10) is associated with the 1018 frame. During the simulation, elements of the roll-pack in contact with the rolls are tracked and their mechanical properties (e.g., stress, and strain) are recorded for every time step.

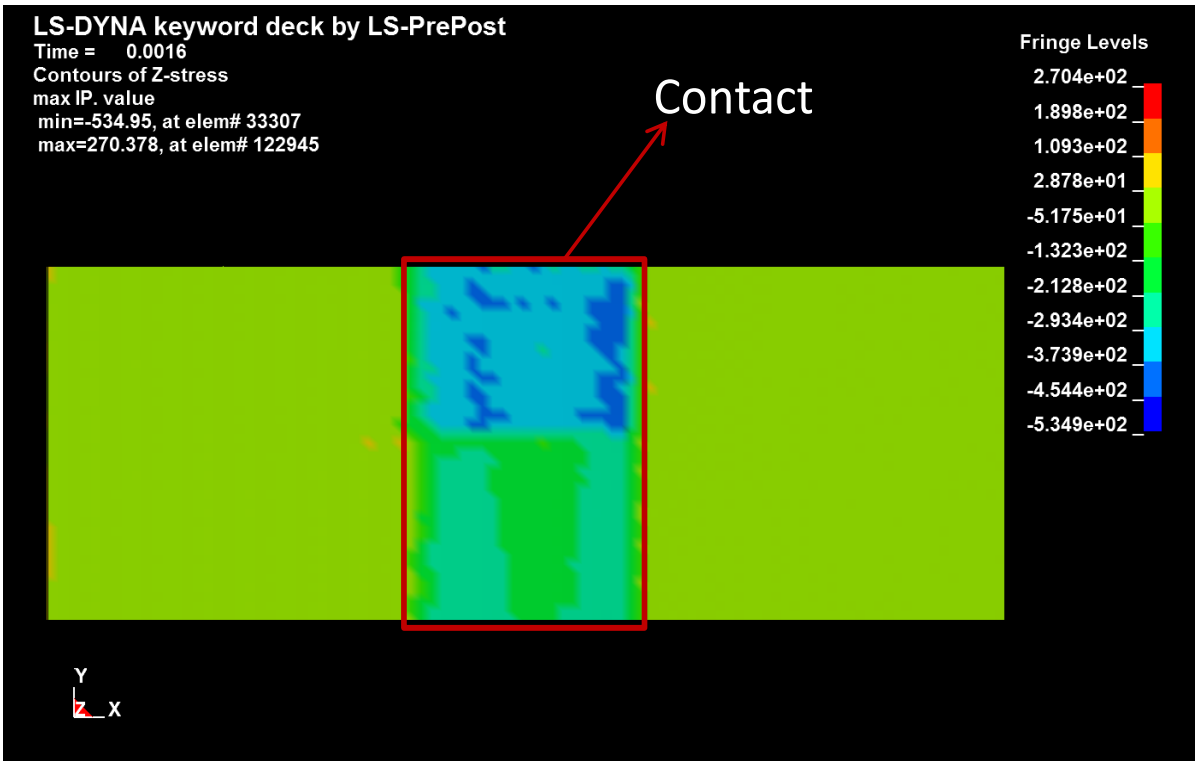

Figure 10. Top View of the Roll-Pack. Contours of vertical stress in MPa (out of plane in z-direction).

4.1.3 Model Validation

Simulations were carried out following Schedules A and B. 15 passes were simulated with a restart and modification of the roll settings and rotation direction between every two passes. The roll-separation force after each pass was calculated from the model and values compared to experimental measurements (Figures 11 and 12 for Schedules A and B, respectively). Figures 11 and 12 both include a predicted entry temperature of the roll-pack, which takes into account the radiation with the ambient surroundings, conduction due to contact of the rolls, and an assumed

temperature loss of 15°C to radiation. The temperature is an average value at the cross section of the roll-pack in the middle of the rolling reduction.

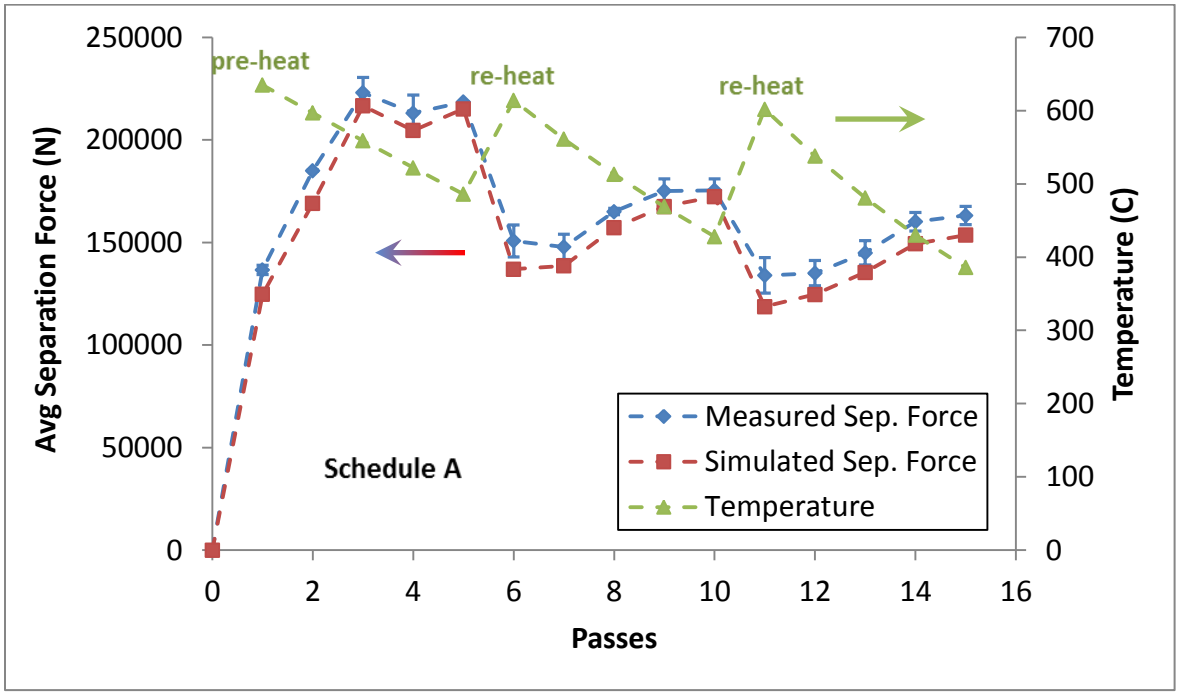

Figure 11. Measured Separation Forces Compared to Simulated Separation Forces for the First 15 Passes of Schedule A

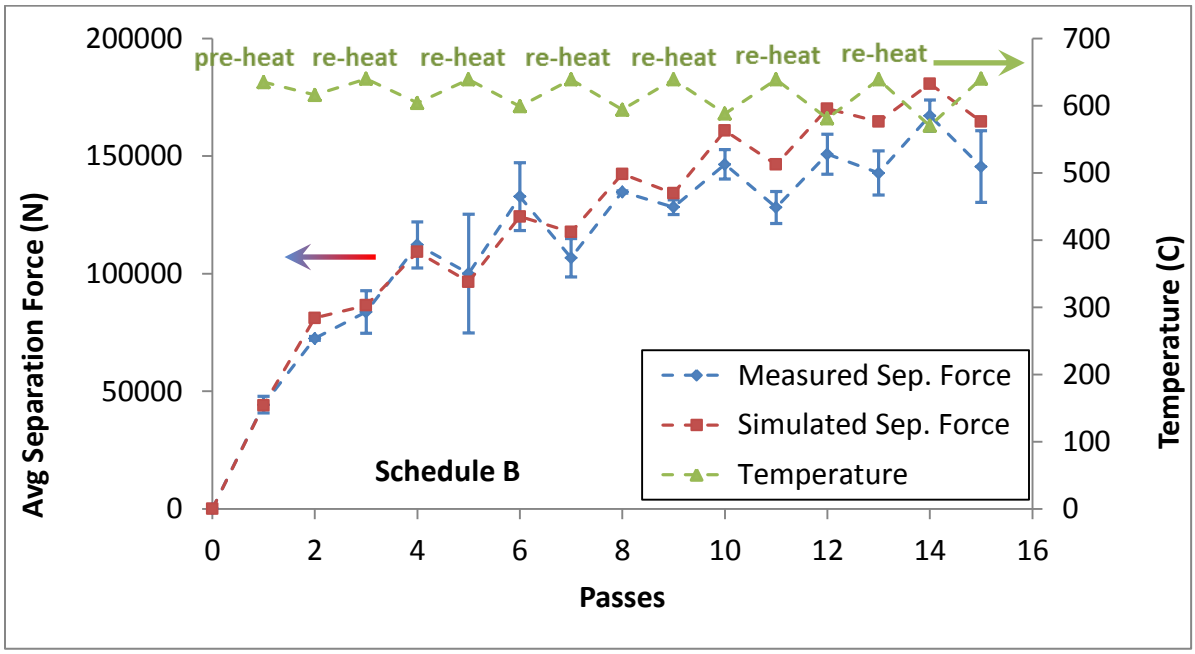

Figure 12. Measured Separation Forces Compared to Simulated Separation Forces for the First 15 Passes of Schedule B.

For both Schedules A and B, model simulations were performed using U-10Mo mechanical properties from the literatures where U-10Mo was considered perfectly plastic with no work-hardening in the 400^{o}C to 650^{o}C temperature range. The model prediction is in good agreement with the experimental measurements. For Schedule A, the predicted forces deviate less than 7 percent over the entire rolling schedule. For Schedule B, a slight divergence appears after Pass 6; the deviation (an over-prediction of force) reaches a maximum (14 percent) at the last pass. Given that the forces in the early passes for Schedule B are in close agreement, this divergence may be related to a change in the U-10Mo or 1018 microstructure resulting in a decreased flow stress not accounted for in the U-10Mo or 1018 constitutive relation. This deviation may be more likely in Schedule B where longer times at elevated temperature could have resulted in microstructural changes (e.g., homogenization of any second phases or recrystallization). There is also a difference in temperature loss for Schedule A compared to Schedule B; about 250°C as the roll-pack thins. Further, the difference in separation force curves between Schedules A and B should be noted; Schedule A is in three steps and Schedule B is serrated due to the difference in reheat frequency. Roll-separation force is clearly observed to decrease every time the roll-pack is reheated and correlates well to the measured values for force.

Simulations were also conducted for Schedule A using U-10Mo mechanical properties obtained from compression tests performed at PNNL and reported in Joshi et al. (2013). Figure 13 represents a comparison between measured rolled separating force, and model predictions using properties from the literature (Simulated Separation-Force 1) and from PNNL compression tests (Simulated Separation-Force 2). Taking into account the material work-hardening for temperatures below 550°C was reflected on the simulated roll-separating force which is in a better agreement with the measurements. We can clearly observe the shift to the top of the roll-separating force curve after introducing the work-hardening observed in compression tests. Note that the predicted forces using PNNL compression data deviate less than 3 percent over the entire rolling schedule whereas the predicted forces using literature data ~7 percent deviation from the measurements.

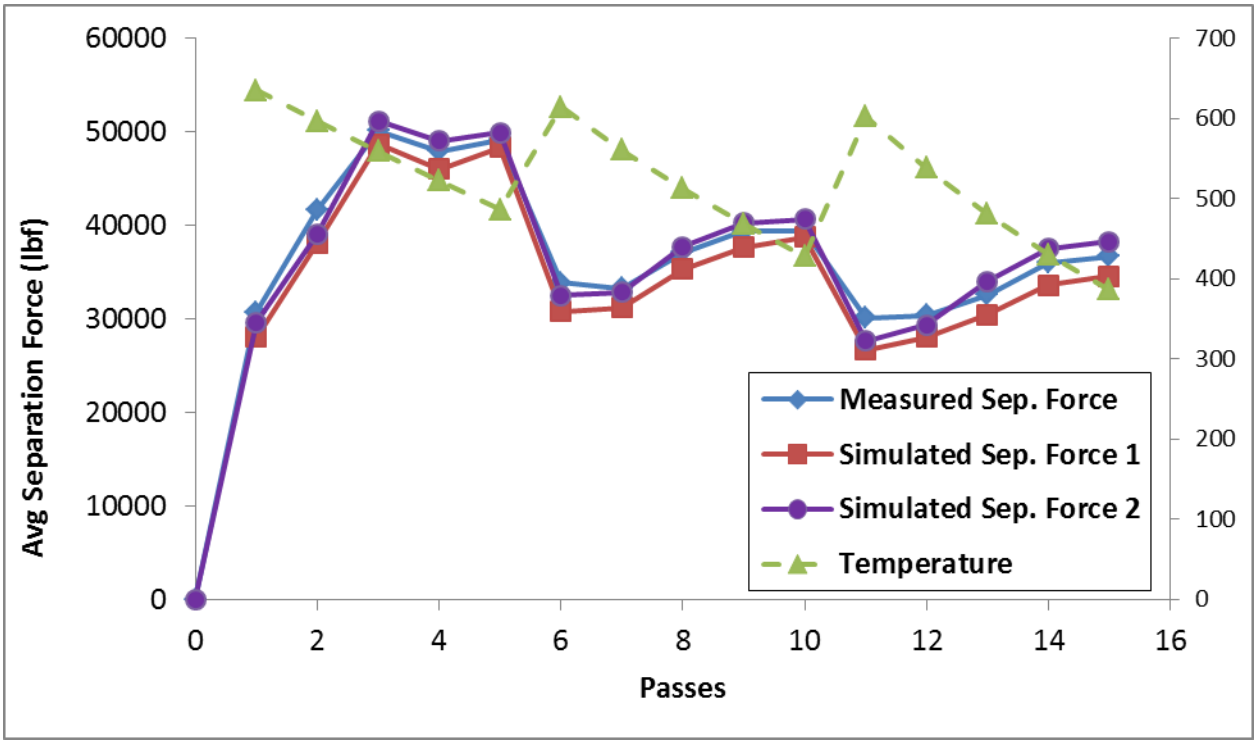

Figure 13. Measured Separation Forces Compared to Simulated Separation Forces (using mechanical properties from 1) the literature and 2) PNNL compression tests) for the First 15 Passes of Schedule A

Figures 14 and 15 represent the predicted and measured roll-pack thickness after every pass for Schedules A and B, respectively. These measurements were taken at the center of the roll-pack. Both Schedules A and B show a good agreement between the model prediction and measurements; however a slight underestimation exists for the simulated thickness as compared to the measured value. This underestimation is very slight and likely due to difficulties in making accurate thickness measurements on hot sheets that are not flat. The difference may be entirely related to the accuracy of the measurement; however, in this simulation rolls are considered rigid and non-deforming whereas in actual rolling operations the yokes will elastically stretch (buck) and the rolls will elastically flatten. Both buck and flattening will result in a thicker sheet; therefore, under-prediction of thickness may be expected.

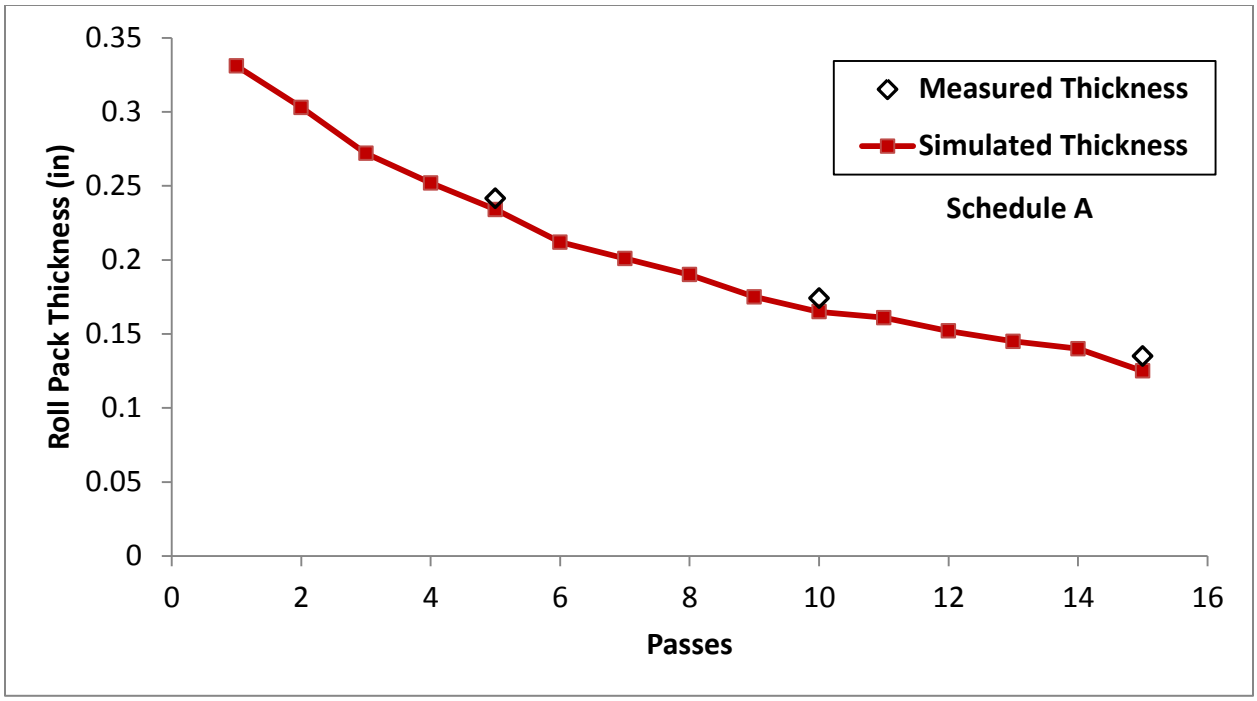

Figure 14. Roll-Pack Thickness for the First 15 Passes for Schedule A

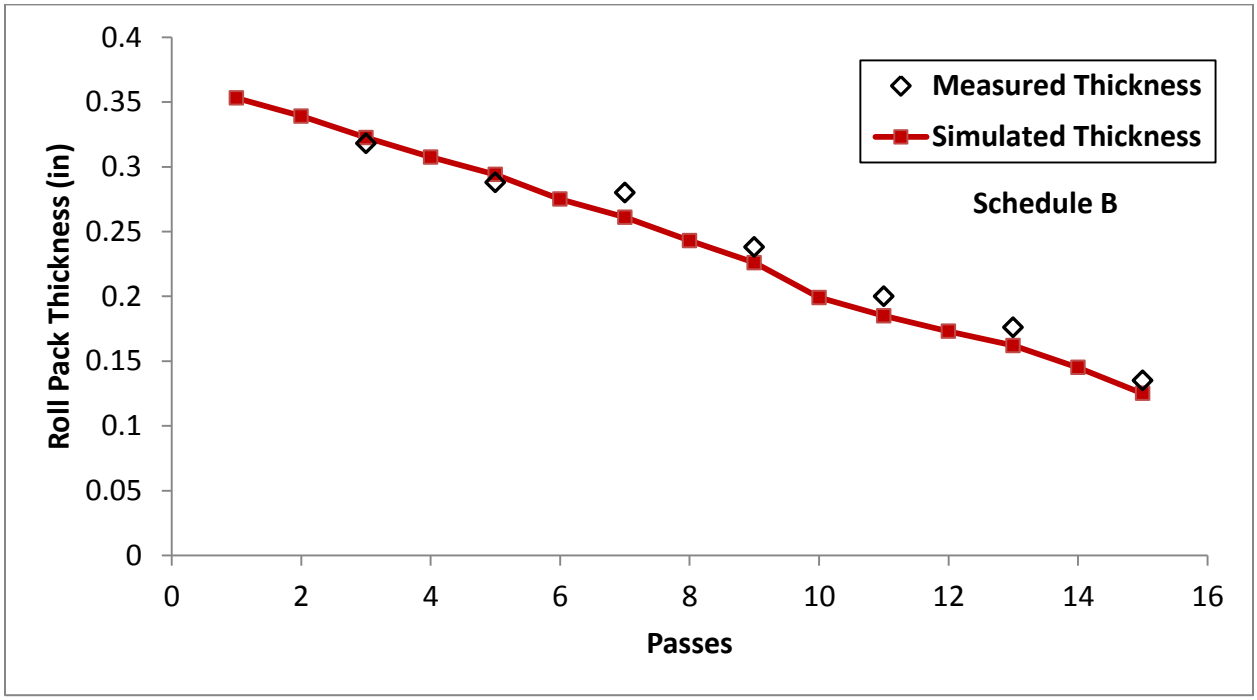

Figure 15. Roll-Pack Thickness for the First 15 Passes for Schedule B.

4.2 Predicted Rolling Defects

Achieving a uniform thickness of U-10Mo foil is a major objective of this rolling process. A closer look at the first set of simulation results, used for the model's validation, revealed the presence of localized thickening (dog-boning) at both ends of the U-10Mo sheet within the 1018 can. To quantify the observed dog-boning in the simulations, the thickness variation along the centerline of the U-Mo sheet for both Schedules A and B was plotted in Figure 16. Thickness is measured at 50 equidistant points from one end of the coupon to the other, along the mid-plane of the alloy coupon lengthwise. Dog-bone areas show an ~25 and 23 percent thickness increase with respect to the average thickness in the remaining part of the coupon for Schedules A and B, respectively.

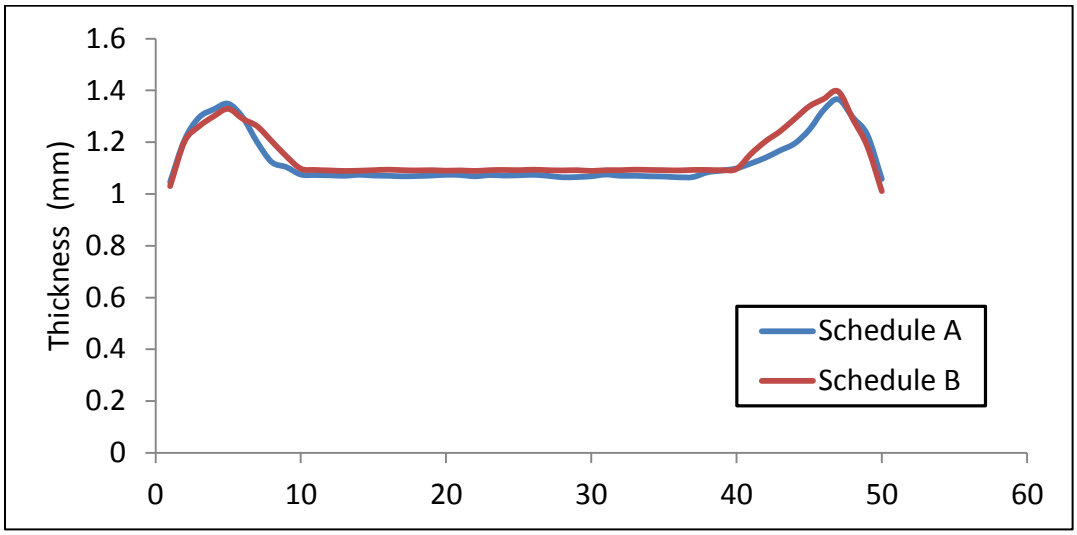

Figure 16. Thickness Variation Along the Coupon for Schedules A and B.

Dog-boning is considered as one the major issues of rolling a fuel coupon inside a picture-frame type of can and has been observed in actual rolled U-Mo fuels. This highly undesirable effect likely results from the difference in yield strength between the 1018 steel material (can) and the U-10Mo (fuel coupon). Dog-boning occurs when the sheet pack first enters the rolls and the separation force is entirely a result of rolling the 1018 can. As the U-10Mo enters the roll pinch zone, it only makes up a small fraction of the material being rolled. As the 1018 pulls, via friction, the U-10Mo into the rolls, a gap begins to form between the 1018 can and the U-10Mo sheet. The harder U-10Mo acts as a non-deformable mandrel and the 1018 flows past the U-10Mo, forming a gap between the can and the U-10Mo as observed in the FEM (see Figure 17). Once the tension and roll pinching is sufficient to pull the U-10Mo into the rolls, the 1018 can has been thinned and the U-10Mo rolls to a thicker dimension forming the thick end of the dog-bone. As the U-10Mo is rolled, the entire 1018 can is pulled into the rolls and the U-10Mo

becomes thinner. A different combination of materials, with less yield strength differential between the fuel and the can, might be an efficient way to reduce dog-boning.

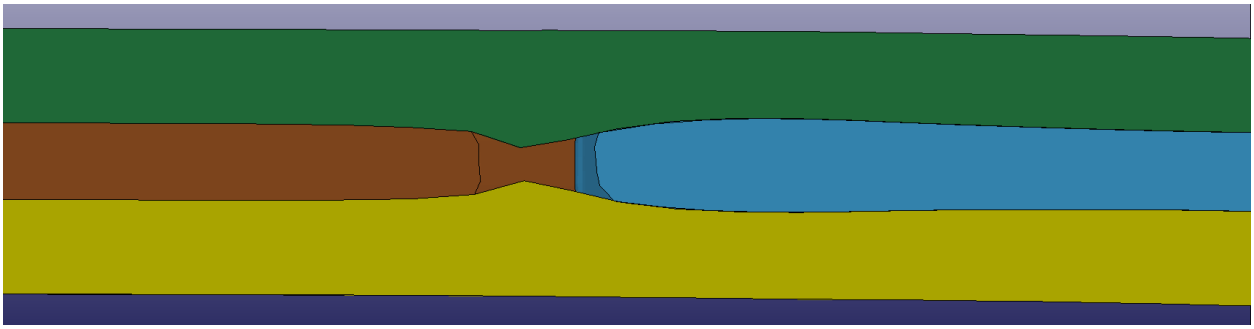

Figure 17. Gap Formed between the End of the U-Mo Coupon and the 1018 Can

The FEM simulation, using a rigid non-distorting roll stand may over-predict the dog-boning; however dog-boning was observed in all co-rolled U-10Mo sheet packs. This defect results in the need for trimming to ensure uniform thickness and an associated yield loss.

Because rolling defects were observed in the simulation predictions for both schedules, such as dog-boning, waviness, and thickness non-uniformity. A parametric study on the influence of the cladding material on the rolling defects was conducted following the rolling Schedule A presented in previous sections.

4.2.1 Influence of the Can Material on Dog-boning

Four cases are considered in this parametric study: 1) rolling of a U-10Mo coupon inside a 1018 steel can, 2) rolling of a U-10Mo coupon inside a 304 stainless steel can, 3) rolling of a U-10Mo coupon inside a Zircaloy-2 can, and 4) bare rolling of a U-10Mo coupon. To quantify the observed dog-boning in the simulations, the thickness variation along the centerline of the U-10Mo sheet was plotted in Figure 18. Thickness is measured at 50 equidistant points from one end of the coupon to the other, along the mid-plane of the alloy coupon lengthwise. Dog-bone areas show a ~25 percent thickness increase with the respect to the average thickness in the remaining part of the coupon for the 1018 steel can. About 19 percent thickness increase is observed in the case of rolling inside the 304 stainless steel can, whereas only ~15 percent thickness increase at the edges of the U-10Mo coupon is observed in the case of rolling inside a Zr can. The bare rolling case does not show any dog-boning defect and we can observe a relatively uniform thickness along the coupon. Dog-boning amplitude is inversely proportional to the strength of the can material. In fact, the stronger is the can material, the less likely localized thickening of the fuel alloy and thinning of the cladding at the edges of the fuel core are observed.

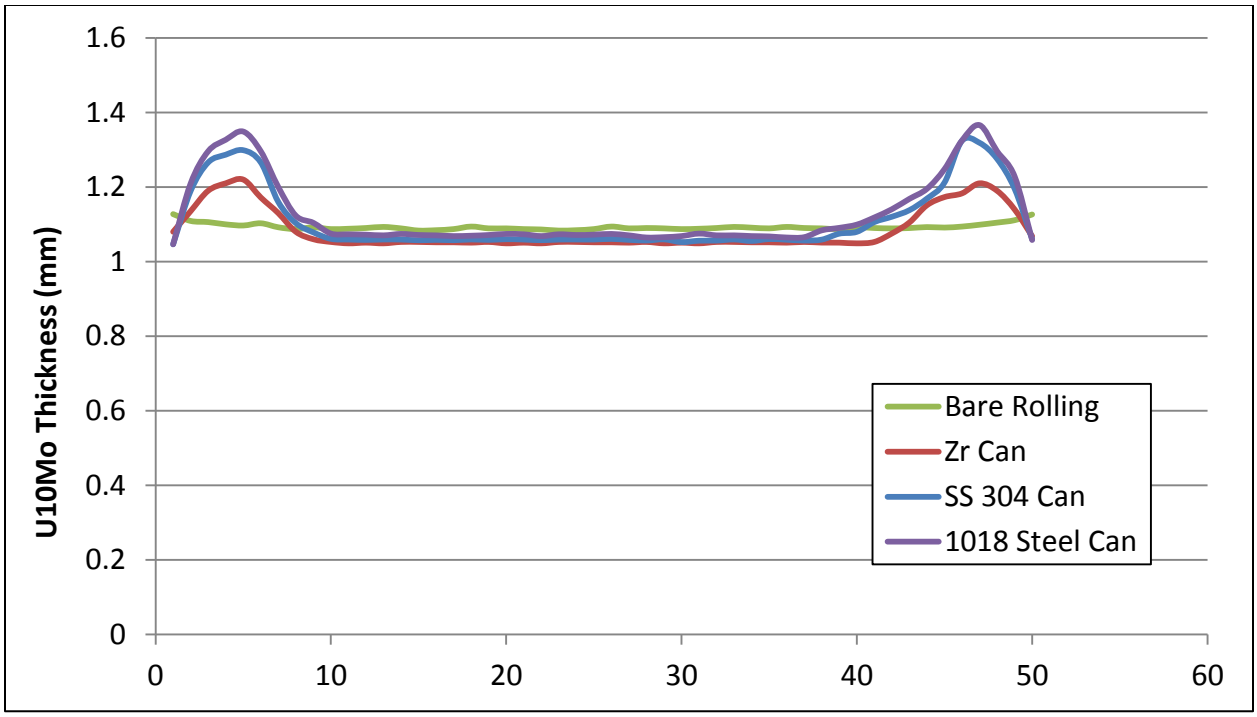

Figure 18. Thickness Variation across the Length of the U-10Mo Coupon in the Cases Of 1) Rolling Inside 1018 Steel Can, 2) Rolling Inside 304 Stainless Steel Can, 3) Rolling Inside Zr-2 Can, and 4) Bare Rolling

Figure 19 represents the gap between the U-10Mo coupon and the picture-frame can material for 1018 steel and Zr-2 can rolling Note that this gap is larger for 'softer' can materials like 1018 carbon steel and thus leads to more thinning of the clad and thus more thickening of the fuel core. Using Zr-2 as a can material reduces the amplitude of dog-boning by ~40 percent, whereas 304 stainless steel represents an intermediate solution to the dog-boning issue. Another way of quantifying the dog-boning is to represent the roll-separation force before, during, and after the pinch zone at the extremity of the fuel core.

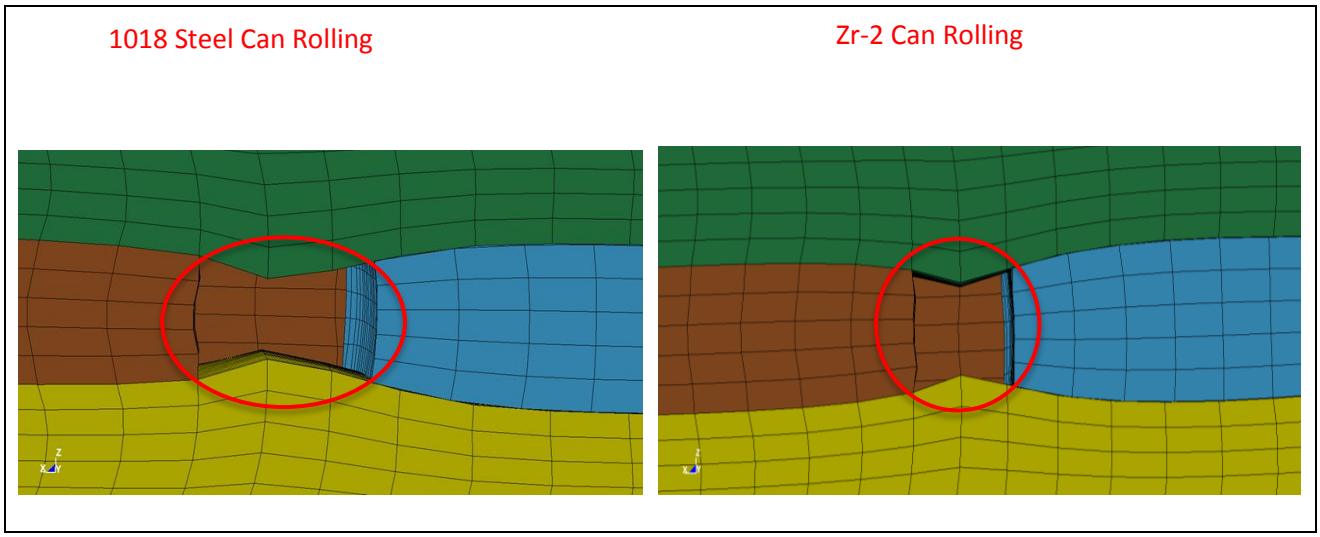

Figure 19. Gap between the U-10Mo Coupon and the Picture-Frame Can Material for 1018 Steel and Zr-2 Can Rolling

Thickness variation was also monitored along the width of the rolled sheet. Except for the areas near the edges where dog-boning was observed, the thickness is uniform along the width of the U-10Mo coupons. Figure 20 shows an isometric view, with a cross section in the middle along the width, of the rolled sheet after 10 passes in the case of the Zr-2 can. Dog-boning near the edge lengthwise is clearly observed, but the thickness does not vary much along the width. Generally, variation in thickness across the width of the rolled sheet is caused by the deformation of the rolls. Because we are modeling the rolls as rigid bodies, no roll flattening or roll bending under load is allowed.

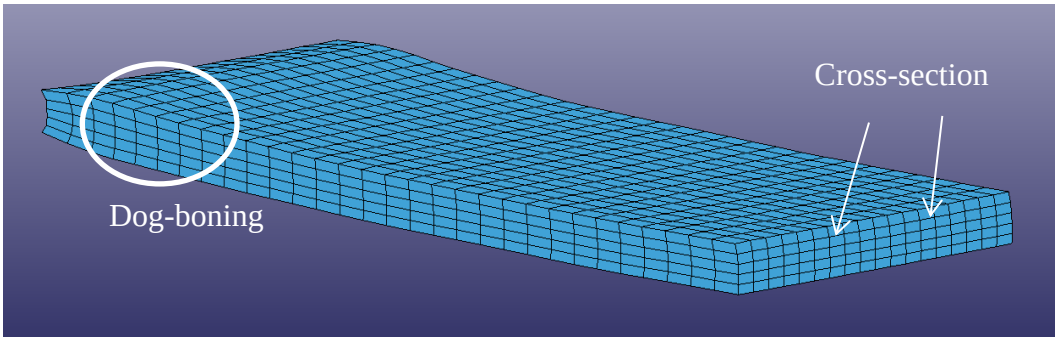

Figure 20. Isometric View of the U-10Mo Coupon, Cross-Sectioned in the Middle Widthwise, after 10 Passes in the Case of Zr-2 Can

4.2.2 Influence of the Can Material on Waviness

Waviness of the rolled sheet pack is also observed in canned fuel rolling. Figure 21 presents a comparison of the U-10Mo coupons rolled inside a 1018 steel can, inside a Zr-2 can, and in the case of bare rolling. This waviness has been measured and represented in Figure 22. The picture in the plot represents a longitudinal cross section of the U-10Mo coupon along middle line. Point #1 is located at the left bottom corner of the cross section. Vertical distance between point #1 and point # {2 ..13}, all located at the bottom surface of the alloy coupon, have been measured and values reported on the plot. Waviness is more pronounced in the case of 1018 can rolling compared to 304 stainless steel can and Zr-2 can rolling, whereas almost no waviness is present in the bare rolling case. In general, this defect can result from various aspects of the rolling process including bending of the rolls, variation of the roll-separation force along the sheet, dog-boning, etc. As stated before, since no deformation of the rolls is present in our modeling approach, we will only focus on waviness causes other than bending and flattening of the rolls. The gap between the fuel core and the can picture frame appears to be the major contributor to this defect. This gap results from the mismatch of strength between the U-10Mo coupon and the can material. A sudden change of the material resistance, when the rolls reach the fuel core, leads to an increase in the roll-separation force and therefore to the initiation of the waviness of the sheet. Figure 21 also shows the relatively uniform bare-rolled U-10Mo coupon. No dog-boning, no waviness, and no thickness variation in any direction are present in the predicted rolled sheet.

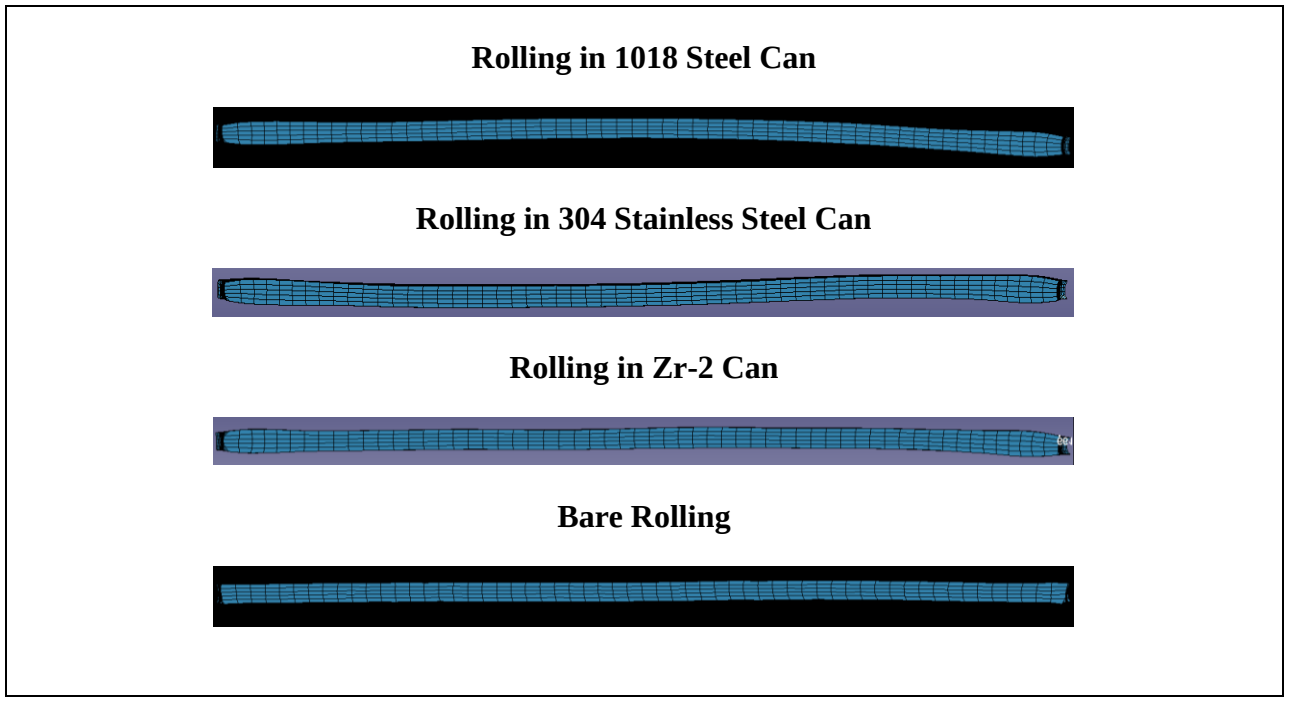

Figure 21. Shape of the Rolled U-10Mo Coupons after 15 Passes

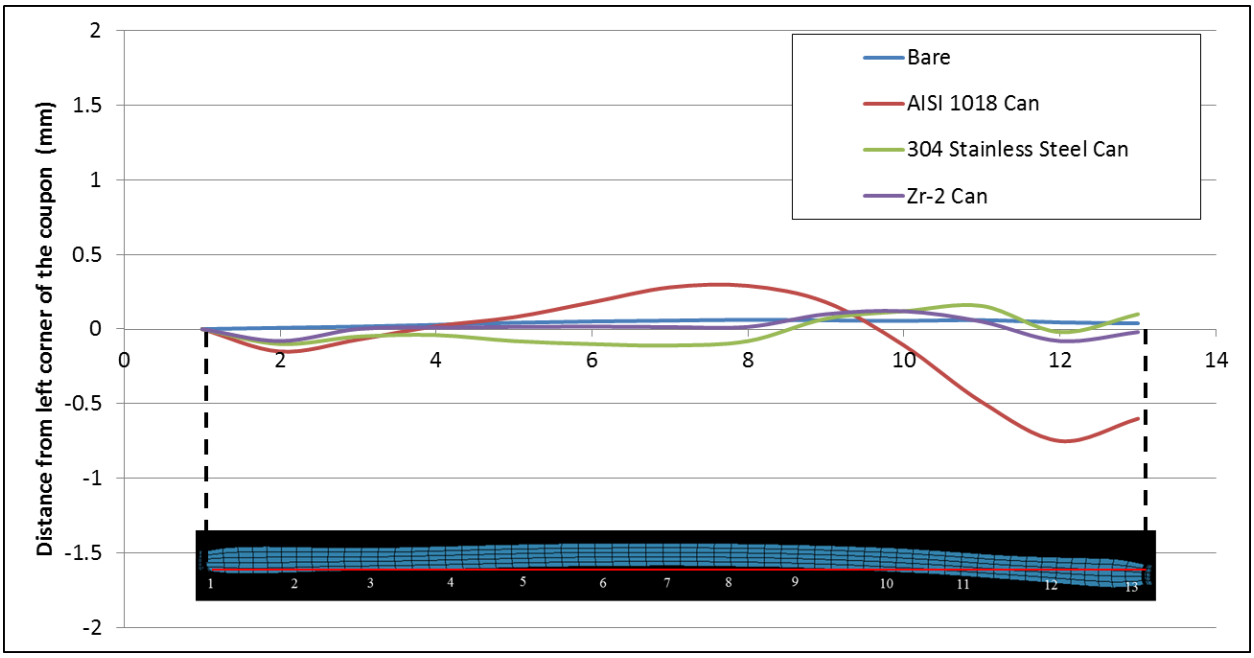

Figure 22. Representation of the Waviness of the U-10Mo Coupon

5.0 Summary

- An FEM of the pack-rolling process of U-10Mo canned in 1018 steel was produced and shown to correlate well to experimental roll-separation forces and pack thickness observed in actual rolling operations.
- Two rolling schedules were simulated: Schedule A used two reheats in 15 passes and Schedule B used seven reheats in 15 passes. The predicted force and thickness for the two-reheat pass deviated less than 7 percent from the measured values. The seven-reheat schedule showed a steadily increasing over-prediction of the separation force to a maximum variation of 14 percent. The close correlation with early passes of Schedule A and the entire two-reheat schedule indicates that the increased time and temperature causes a change in the microstructure of the U-10Mo or 1018 steel. This change in mechanical behavior with time at temperature has not been investigated and is not accounted for in the constitutive relations for either U-10Mo or 1018 steel.
- Model simulations using U-10Mo properties from PNNL compression tests show that predicted roll-separating force is slightly higher for temperatures below 550^{o}C because of the work-hardening induced in the material. We also observe that the predicted roll-separating force overall is in a better agreement with the measurements.
- The model of the pack-rolling process was used to explain a defect commonly found in the pack rolled sheets known as dog-boning. This defect results in non-uniform sheet thickness and has been attributed to a mismatch in flow stress of the 1018 steel and the U-10Mo at the ends of the roll-pack. Using a can material with a flow stress that more closely matches that of U-10Mo would likely reduce or eliminate dog-boning.
- Dog-boning in the core fuel was observed and quantified in this study. Dog-bone areas show ~25 percent, ~19 percent, and ~15 percent thickness increases with the respect to the average thickness in the remaining part of the coupon for the 1018 steel can, the 304 stainless steel can, and the Zr-2 can, respectively.
- Waviness follows the same trend as for dog-boning and is more pronounced in the case of rolling inside the 1018 steel can, followed by the 304 stainless steel can, then the Zr-2 can. Using a can material with a flow stress that more closely matches that of U-10Mo would likely reduce or eliminate both dog-boning and waviness. Bare rolling case simulations show an almost perfect foil with almost no waviness.
- The model predictions indicated that reducing the mismatch in strength between the can material and the fuel core leads to less defects.
- The model is being used currently to perform a parametric study on the impact of roll diameter, temperature, and reductions on through thickness strain variations and roll-separating forces.

6.0 References

AN-176, 1960. Final Report on Conceptual Design and Initial Radiological Safety Study for a Pulsed Nuclear Reactor, s.l.: s.n.

Avitzur, B., 1982. Handbook of Metal-Forming Processes. s.l.:Wiley-Interscience.

Azushima, A., Nakata, Y. & Toriumi, T., 2010. Prediction of effect of rolling speed on coefficient of friction in hot sheet rolling of steel using sliding rolling tribo-simulator. Journal of Materials Processing Technology, 210(1), pp. 110-115.

Burkes, D. E., Hartmann, T., Prabhakaran, R. & Jue, J.-F., 2009. J. Alloys Compd., Volume 479, pp. 140-147.

Burkes, D. E. et al., 2010. Journal of Nuclear Materials, Volume 403, pp. 160-166.

Chavez, S., Korth, G. E., Harper, D. M. & Walker, T. J., 1994. High-temperature tensile and creep data for Inconel 600, 304 stainless steel, and SA106B Carbon steel. Nuclear Engineering and Design, 148(2-3), pp. 351-363.

Chen, J. & Young, B., 2006. Stress-strain curves for stainless steel at elevated temperatures. Engineering Structures, 28(2), pp. 229-239.

Clauss, F. J., 1969. Engineer's Guide to High-Temperature Materials. s.l.:Addison-Wesley.

D'Amours, G. & Béland, J. F., 2011. Warm Forming Simulation of 7075 Aluminium Alloy. Strasbourg, France, s.n.

Farkas, M. S., 1967. Mechanical and Physical Properties of Fuels and Cladding Materials With Potential for Use in Brookhaven's Pulsed Fast Reactor, s.l.: Part I, BMI-X-455.

H. E. Boyer, T. L. G., 1985. Metals Handbook. Materials Park ed. OH: American Society for Metals.

Hwu, Y. & Lenard, J. G., 1988. Trans. ASME J. Eng. Mater. Tech., Volume 110, p. 22–26.

Joshi, V., Nyberg, E., Lavender, C., Paxton, D., Garmestani, H., Burkes, D. Thermomechanical process optimization of U-10 wt% Mo – Part 1: high-temperature compressive properties and microstructure. Journal of Nuclear Materials, In press. 2013

Knight, C. W., Hardy, S. J., Lees, A. W. & Brown, K. J., 2005. Influence of roll speed mismatch on strip curvature during the roughing stages of a hot rolling mill. Journal of Materials Processing Technology, 168(1), pp. 184-188.

Komori, K., 1988. Analysis of cross and vertical buckling in sheet metal rolling. International Journal of Mechanical Sciences, 40(12), p. 1235–1246.

Komori, K., 1996. Analysis of herring-bone mechanism in sheet rolling. Journal of Materials Processing Technology, 60(1-4), p. 377–380.

Lee, D. B., Kim, K. H. & Kim, C. K., 1997. J. Nucl. Mater, Volume 250, p. 79–82.

McPherson, B., 1958. The Determination of True Stress – True Strain Curves and Modulus of Elasticity of a Uranium – 10 w/o Molybdenum Alloy at Elevated Temperatures, s.l.: AECU-3801.

Meyer, M. K. et al., 2002. J. Nucl. Mater., Volume 304, pp. 221-236.

Moore, G. A. & Marshall, M. C., 2010. Co-Rolled U10Mo/Zirconium-Barrier-Layer Monolithic Fuel Foil Fabrication Process - INL Report, s.l.: s.n.

Nepershin, R. I., 1999. Int. J. Mech. Sci., pp. 1401-1421.

Ozaltun, H., Shen, M. H. H. & Medvedev, P., 2011. Journal of Nuclear Materials, 419(1-3), pp. 76-84.

Park, J. M. et al., 2001. J. Met Mater Int., 7(2), p. 151–157.

Pasqualini, E. E., 2008. MONOLITHIC UMo NUCLEAR FUEL PLATES WITH NON ALUMINIUM CLADDING. Hamburg, Germany, RRFM Euronuclear.

Peterson, C. A. W. & Vandervoort, R. R., 1964. Stress-Cracking in the Uranium-10 w/o Molybdenum Alloy, s.l.: University of California Lawrence Radiation Laboratory Report UCRL-7767.

Seredynski, F., 1973. Prediction of Plate Cooling During Rolling-Mill Operation. J. Iron and Steel Inst., pp. 197-203.

Seredynski, F., 1973. Prediction of Plate Cooling During Rolling-Mill Operation. J. Iron and Steel Inst., pp. 197-203.

Shapiro, A., 2007. Using LS-DYNA for hot forming. Frankenthal, Germany, s.n.

Shapiro, A., 2009. Using LS-DYNA for hot stamping. Salzburg, Austria, s.n.

Shuai, M. R., Huang, Q. X. & Zhu, Y. C., 2010. Finite Element Simulation of the Hot-Rolling Process of Titanium Alloy Bar. Advanced Materials Research , Volume 145, pp. 181-186.

Snelgrove, J. L. et al., 1997. Nucl. Eng. Des., Volume 178, pp. 119-126.

Soulami, A., Burkes, D., Lavender, C. & Paxton, D., 2013. Finite-Element Model to Predict Roll-Separation Force During Rolling of U-10Mo Alloys. Submitted for publication in Journal of Materials Processing Technology.

Thurber, W. & Beaver, R., 1959. Development of silicon-modified 48 wt % U-Al, s.l.: Oak Ridge National Laboratory.

Tieu, A. K., Jiang, Z. Y. & Lu, C., 2002. A 3D finite element analysis of the hot rolling of strip with lubrication. Journal of Materials Processing Technology, Volume 125–126, p. 638–644.

Waldron, M. B., Burnett, R. C. & Pugh, S. F., 1958. The Mechanical Properties of Uranium-Molybdenum Alloys, s.l.: AERE-M/R-2554.

Whitmarsh, C. L., 1962. Review of Zircaloy-2 and Zircaloy-4 properties relevant to N. S. Savannah reatcor design, s.l.: Oak Ridge National Laboratory.

ZHANG, D. F., DAI, Q. W., FANG, L. & XU, X., 2011. Prediction of edge cracks and plastic-damage analysis of Mg alloy sheet in rolling. Trans. Non-ferrous Met. Soc. of China, pp. 1112-1117.

Distribution

No. of Copies

1 Department of Energy
National Nuclear Security Administration
Global Threat Reduction Initiative
1000 Independence Ave.
Washington, D.C. 20002-USA
Mr. Christopher Landers
Dr. Natraj Iyer (PDF)

1 Idaho National Laboratory
P.O. Box 1625
Idaho Falls, ID 83415
Mr. Kenneth Rosenberg
Dr. Mitchell Meyer (PDF)

2 Argonne National Laboratory
9700 S. Cass Ave.
Argonne, IL 60439
Dr. John Stevens
Dr. Erik Wilson

No. of Copies

4 **Local Distribution**
Pacific Northwest National Laboratory

D.E. Burkes	K8-34
D.M. Paxton	K2-03
C.A. Lavender	K2-03
A Soulami	K2-03

Pacific Northwest
NATIONAL LABORATORY

Proudly Operated by **Battelle** *Since 1965*

U.S. DEPARTMENT OF
ENERGY

902 Battelle Boulevard
P.O. Box 999
Richland, WA 99352
1-888-375-PNNL (7665)
www.pnnl.gov